J Mater Sci (2011) 46:4336–4342
DOI 10.1007/s10853-011-5304-3

IIB 2010

Transmission electron microscopy investigation of boundaries between amorphous "grains" in $Ni_{50}Nb_{20}Y_{30}$ alloy

A. A. Mazilkin · G. E. Abrosimova · S. G. Protasova · B. B. Straumal · G. Schütz · S. V. Dobatkin · A. S. Bakai

Received: 29 August 2010 / Accepted: 18 January 2011 / Published online: 8 February 2011

Abstract Some of the authors of this article recently demonstrated that severe plastic deformation permits the production of metallic alloys containing two coexisting amorphous phases from the crystalline multiphase $Ni_{60}Nb_{18}Y_{22}$ alloy. The aim herein is to provide a detailed description of the microstructure of this system of coexisting amorphous phases by transmission electron microscopy (TEM) analysis. As-cast $Ni_{50}Nb_{20}Y_{30}$ alloy was coarse grained and contained mainly NiY phase (grain size 25 μm) as well as $NbNi_3$, Ni_2Y, Ni_7Y_2, and Ni_3Y phases (grain size 3–5 μm). High-pressure torsion (4 GPa, 10 torsions) completely changed the structure. After severe plastic deformation (SPD), the sample contained two glassy phases and two other nanocrystalline NiY and $Nb_{15}Ni_2$ phases (grain size about 20 nm). Bright-field TEM micrographs showed fine, 5–10 nm, round bubbles of bright Y-rich amorphous phase embedded in darker Nb-rich "grains." In turn, the dark Nb-rich grains were separated by layers of bright Y-rich amorphous phase a few nanometers thick. This stricture permits one to speak about mutual wetting of "grain boundaries" in both amorphous phases.

A. A. Mazilkin · G. E. Abrosimova · S. G. Protasova · B. B. Straumal (✉)
Institute of Solid State Physics, Russian Academy of Sciences, 142432 Chernogolovka, Moscow District, Russia
e-mail: straumal@issp.ac.ru; straumal@mf.mpg.de

A. A. Mazilkin · S. G. Protasova · B. B. Straumal · G. Schütz
Max-Planck-Institut für Metallforschung, Heisenbergstrasse 3, 70569 Stuttgart, Germany

S. V. Dobatkin
A.A. Baikov Institute of Metallurgy and Materials Science, RAS, Leninsky prosp. 49, 117991 Moscow, Russia

A. S. Bakai
NSC Kharkiv Institute of Physics and Technology, Akademichna st. 1, Kharkiv 61108, Ukraine

Introduction

Grain boundaries (GBs) exist in almost all crystalline materials and control the properties of polycrystals, especially when micro- or nanograined [1, and references therein]. Moreover, GBs can be defined [2–8] and observed [9, 10] not only for contact between two misoriented crystals but also for two amorphous "grains" (obtained, for example, from different amorphous particles after sintering [9, 10]). The concept of GBs in amorphous materials permits one to model their mechanical properties, in particular slip localization in amorphous materials [2–8]. The definition of GBs in metallic glasses is not as obvious as between two crystalline lattices. However, the contact layers between different glassy volumes possess lower density than the bulk of the "grains" (exactly as for conventional GBs between crystalline grains). They can be formed, for example, by sintering of amorphous particles that condense independently from supersaturated vapor [9, 10].

Wetting of conventional GBs plays an important role in materials science. The simplest case is equilibrium wetting by a liquid phase (melt). The GB is completely wetted if the contact angle between the GB and melt is zero. In this case, the liquid phase has to substitute the GB separating the two grains. The GB is incompletely wetted if the contact angle between the GB and melt is finite. In this case, the GB can exist in equilibrium contact with the liquid phase. Cahn [11] and Ebner and Saam [12] first assumed that a (reversible) transition from incomplete to complete wetting can proceed with increasing temperature, being a true surface phase transformation. The transition

from incomplete to complete GB wetting can be observed if the energy of the two solid–liquid interfaces, $2\sigma_{SL}$, becomes lower than the GB energy, i.e., $\sigma_{GB} > 2\sigma_{SL}$. Cahn's [11] idea was the motivation for experimental findings of GB wetting phase transformations, initially made in Zn–Sn, Zn–Sn–Pb, and Ag–Pb polycrystals [13, 14]. Later, the original experimental data were reconsidered from this point of view, and numerous indications of GB wetting phase transformations were found, particularly for Zn–Sn, Al–Cd, Al–In, and Al–Pb [15] and W–Ni, W–Cu, W–Fe, Mo–Ni, Mo–Cu, and Mo–Fe [16] polycrystals. The first exact measurements of the temperature dependence of the contact angle with the melt were made using individual GBs in specially grown bicrystals in the Cu–In [17], Al–Sn [18], and Zn–Sn [19] systems.

The phase which wets a GB can be not only liquid but also solid. The transition from incomplete to complete wetting proceeds also in this case [20–23]. However, the equilibration kinetics is very slow in this case. Another important difference is that the transition from incomplete to complete wetting can proceed not only by increasing but also by decreasing temperature [23]. The second phase which wets the GB can be not only liquid or solid but also amorphous. The GB layers of an amorphous phase usually form from the wetting liquid phase during quick cooling [24, 25]. However, there are some indications that the wetting GB layers of an amorphous phase can form also by growth of nanocrystals in an amorphous matrix [26–28]. Can the "GBs" in such an amorphous phase be completely wetted by the layers of a second amorphous phase? This work is devoted to the search for such a phenomenon.

Firstly, to study the wetting of a "GB" in one amorphous phase by a second amorphous phase, we need a sample where two different amorphous phases coexist. Decomposition of one amorphous phase into two or more amorphous phases can proceed either during synthesis or as a result of various treatments of the amorphous phase. In the course of such processes, various amorphous phases form, with different composition and short-order parameters (i.e., the parameters of the locally favoured atomic arrangements with specific spatial symmetry). These amorphous phases usually do not possess distinct (sharp) interfaces, and the decomposition is similar to spinodal decomposition [29]. Amorphous phase decomposition has been observed in various alloys, including $Pd_{74}Au_8Si_{18}$ [29], $Pd_{40.5}Ni_{40.5}P_{19}$ [30], Pd–Si–Sb [31], $Pd_{80}Si_{20}$ [32], $Be_{40}Ti_{24}Zr_{36}$ [33], $Pb_{60}Pd_{40}$ [34], Al–Si–X, Al–Ge–X (X = Ti, Zr, V, W, Mn, Fe, Co, Ni, Cu, Cr, Nb, Mo) [35], Fe–B–P [36], (Au–Pb–Pt)–(Pb–Sb) [37], Zr–Y–Al–Ni [38], $Fe_{40}Ni_{40}P_{14}B_6$ [39], $Fe_{90}Zr_{10}$ [40], $Ni_{70}Mo_{10}P_{20}$ [41], $Ni_{70}Mo_{10}B_{20}$ [42], and Al–Ni–Y [43]. A structural change of the amorphous phase as a result of deformation has been observed in Zr- [43–45] and Al-based alloys [46]. Recently, two-phase amorphous alloys were obtained in several alloy systems: the Zr–La–Al–Ni–Cu system [47], Ni–Nb–Y [48–55], (Ti, Zr)–Y–Al–Co [56–58], Cu–(Zr, Hf)–(Gd, Y)–Al [59], Nd–Zr–Al–Co [60], and Zr–(Cu, Ce, Pr, Nd)–Al–(Ni, Ag) [61–63]. In these materials, decomposition takes place already in the melt, prior to solidification. Recently, metallic glasses simultaneously containing two (or more) different amorphous phases were obtained by severe plastic deformation (SPD) [high-pressure torsion (HPT) mode] of crystalline Ni–Nb–Y alloys [64].

The miscibility gap in the monotectic binary Nb–Y system extends into the ternary Ni–Nb–Y system up to 70 at% Ni as a consequence of the positive mixing enthalpy between Nb and Y [49]. Experimental evidence of phase separation in the melt of $Ni_{58.5}Nb_{20.25}Y_{21.25}$ (numbers indicate at%) has been obtained by in situ X-ray diffraction at elevated temperatures and differential scanning calorimetry [48–51]. The melt in this alloy separated into two immiscible liquid phases already before quenching. Quick cooling of this mixture leads to formation of two amorphous metallic phases from two pre-existing liquid phases [48–51]. The microstructure consists of two amorphous regions, one Nb enriched and the other Y enriched, with a size distribution from several nanometers up to micrometers. From the micrographs published by Mattern et al. [49–51], it is clear that the Y-rich amorphous phase separates the "grains" of the Nb-rich amorphous phase. Therefore, we chose the Ni–Nb–Y alloys for our experiments. In our case, the starting state before HPT is an as-cast alloy consisting of a mixture of crystalline phases; it does not contain any amorphous phase.

Experimental

The $Ni_{50}Nb_{20}Y_{30}$ (numbers indicate at%) alloy which was chosen for these investigations is indicated by the star in the Y–Ni–Nb phase diagram in Fig. 1. In previous work, we investigated the similar alloy $Ni_{60}Nb_{18}Y_{22}$ [64]. Both of these alloys are very close to the composition $Ni_{58.5}Nb_{20.25}Y_{21.25}$ studied previously [49–51]. The compositions of our $Ni_{50}Nb_{20}Y_{30}$ and $Ni_{60}Nb_{18}Y_{22}$ alloys are positioned in the phase diagram slightly to the left and to the right of the composition $Ni_{58.5}Nb_{20.25}Y_{21.25}$ studied previously [49–51]. The $Ni_{50}Nb_{20}Y_{30}$ alloy was prepared by using high-purity components (4 N Ni, 3 N Nb, and 3 N Y) for vacuum induction melting. Alloy pellets (20 g) were melted in a contactless levitation heater at 2500 °C for about 3 min. After melting, the induction heating was switched off, and the melted pellets dropped down into a heavy copper crucible. However, the cooling rate was not fast enough to form the amorphous phase. After grinding,

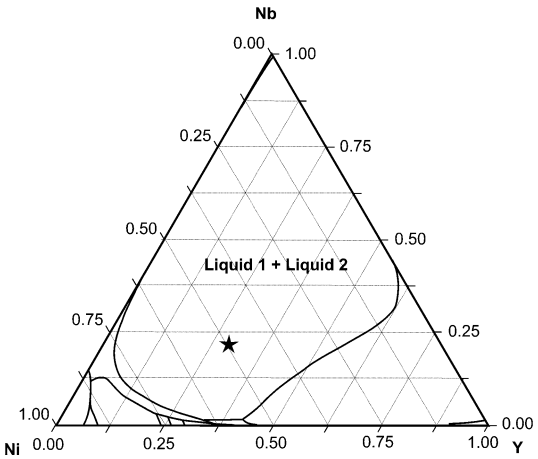

Fig. 1 Liquidus projection of the Y–Ni–Nb ternary phase diagram obtained by the CALPHAD method [66]. The composition of the ternary $Ni_{50}Nb_{20}Y_{30}$ alloy chosen for these investigations is marked by the *star*

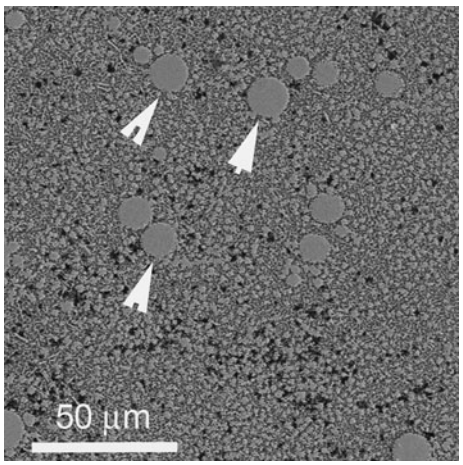

Fig. 3 SEM micrograph of the $Ni_{50}Nb_{20}Y_{30}$ alloy before deformation. Some of the large $NbNi_3$ particles are indicated by *arrow heads*

sawing, and chemical etching, as-cast disks of these alloys, with 10 mm diameter, were subjected to HPT at room temperature under pressure of 4 GPa in a Bridgman anvil-type unit (10 torsions, duration of process about 300 s). X-ray diffraction (XRD) data were obtained by using a Siemens diffractometer (Co K_α radiation). Transmission electron microscopy (TEM) investigations were carried out by using a JEM-100CX microscope at accelerating voltage of 100 kV with TEM samples prepared by mean of ion milling. They were cooled by liquid nitrogen during preparation to avoid changes to their structure. Scanning electron microscopy (SEM) and electron-probe micro-analysis (EPMA) were carried out by using a Zeiss Supra 50VP microscope equipped with a LINK energy-dispersive spectrometer produced by Oxford Instruments. Grain size D was estimated by the Scherrer formula $D = 0.9\lambda/\beta\cos\,\theta$ (where λ is the wavelength, β is the physical line broadening, and θ is the diffraction angle) [65]. The β value was determined by subtracting the broadening of a standard sample from that of the investigated sample. In the case of nanoscale materials, the contribution of the instrumental broadening to the full line width is insignificant.

Results and discussion

The X-ray diffraction spectrum of the $Ni_{60}Nb_{18}Y_{22}$ alloy before deformation is shown in Fig. 2a. The as-cast sample contains several crystalline phases. The spectrum is well described by a deconvolution into the peaks of NiY, $NbNi_3$, Ni_2Y, Ni_7Y_2, and Ni_3Y phases. No contribution from amorphous phase(s) was detected. An SEM micrograph of the as-cast $Ni_{50}Nb_{20}Y_{30}$ alloy is shown in Fig. 3. The microstructure contains large spherical grains of $NbNi_3$ phase (mean grain size about 25 μm) surrounded by a mixture of NiY, Ni_2Y, Ni_7Y_2, and Ni_3Y phases (grain size 3–5 μm). The $Ni_{60}Nb_{18}Y_{22}$ alloy [64] contained the same

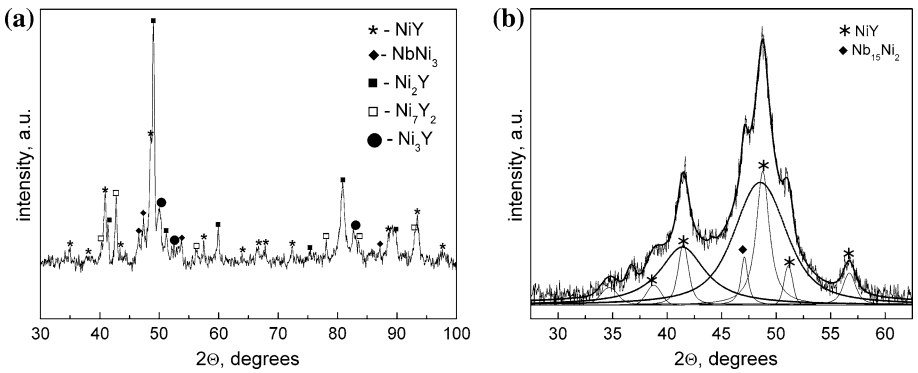

Fig. 2 **a** X-ray diffraction spectrum of the $Ni_{50}Nb_{20}Y_{30}$ alloy before deformation. The main phase component is the NiY phase. Other phases are $NbNi_3$, Ni_2Y, Ni_7Y_2, and Ni_3Y. **b** X-ray diffraction spectrum of the $Ni_{50}Nb_{20}Y_{30}$ alloy after HPT, consisting of two halos corresponding to two amorphous phases (*thick lines*), superimposed on the peaks of the crystalline phases NiY and $Nb_{15}Ni_2$ (*thin lines*)

phases as the $Ni_{50}Nb_{20}Y_{30}$ alloy, but in slightly different volume ratios. The $Ni_{60}Nb_{18}Y_{22}$ alloy [64] contained more nickel than the present alloy or samples of $Ni_{58.5}Nb_{20.25}Y_{21.25}$ quenched from the liquid state [49–51]. Unfortunately, few experimental data on the ternary Y–Ni–Nb phase diagram are available. The phase diagram (Fig. 1) was calculated using CALPHAD [49, 66]. In our experiments, as well as in previous study [48–52], no ternary phases were observed. Ternary Y–Ni–Nb phases are also absent from the existing databases [67, 68].

HPT completely changed the structure. No indications of the $NbNi_3$, Ni_2Y, Ni_7Y_2, and Ni_3Y phases present in the starting coarse-grained alloy were observed in the sample after HPT. Only the NiY crystalline phase, which also existed in the as-cast state but with somewhat different parameters, remained after the deformation. The corresponding XRD pattern is shown in Fig. 2b, showing the partly superimposed halos of the two amorphous phases with maxima at $q_1 = 25.1\ nm^{-1}$ ($2\theta_1 = 41.4°$) and $q_2 = 28.8\ nm^{-1}$ ($2\theta_2 = 48.6°$) and peaks of two other crystalline NiY and $Nb_{15}Ni_2$ phases. These values are very close to the halo positions ($q_1 = 26.3\ nm^{-1}$ and $q_2 = 29.5\ nm^{-1}$) observed in the quenched alloys [49]. The area under the scattering curve corresponding to the amorphous phase with $q_2 = 28.8\ nm^{-1}$ (and also the amount of this phase) is about three times higher than that of the amorphous phase with $q_1 = 25.1\ nm^{-1}$. The maximum for the larger scattering vector is slightly higher, as also reported for the quenched alloys [49]. The peak broadening of the phases permits estimation of their grain size as about 20 nm. Both the Ni_2Y and Nb_6Ni_7 phases exist in equilibrium below 1000 °C [49].

After HPT, the samples were inhomogeneous and contained mainly either crystalline or predominantly amorphous areas, both of which were equiaxial, with size of about 500–1000 nm, and randomly mixed in the sample. In other words, the size of these areas was at least one order of magnitude higher than the grain size of all crystalline phases before HPT (Fig. 3). We did not observe any pronounced nonuniformity, such as shear bands, in the shape or spatial distribution of the crystalline or amorphous areas. The detailed mechanism of the formation of crystalline or amorphous areas during HPT is still unclear and will be the subject of detailed investigation in the future (for example, by stepwise increase of the degree of deformation as in [69]).

Figures 4 and 5 show TEM micrographs of the sample after HPT. Figure 4 shows a bright-field image of an amorphous part of the sample. There are no diffraction rings corresponding to the crystalline phases, and only an amorphous halo appears in the selected-area electron diffraction (SAED) pattern. However, it is not symmetric and can be separated into two halos (see the inset to Fig. 4,

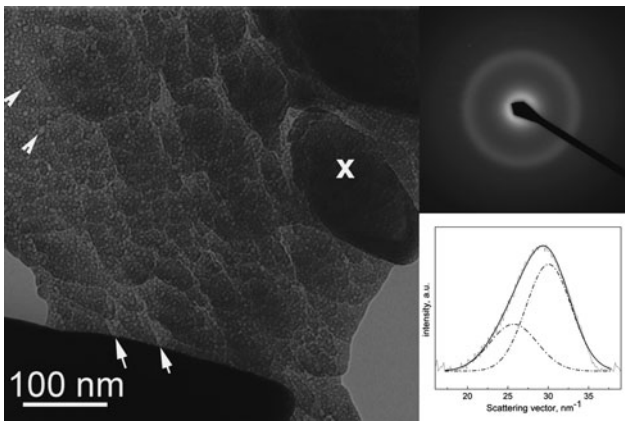

Fig. 4 Bright-field TEM micrograph of the $Ni_{50}Nb_{20}Y_{30}$ alloy after HPT taken from a predominantly amorphous area. *X* marks a large grain of Nb-rich amorphous phase (appears dark). *Arrows* in the *left part* of the micrograph indicate small bubbles of Y-rich amorphous phase (appear bright). *Arrows* in the *bottom part* of the micrograph indicate layers of Y-rich amorphous phase (appear bright) between large grains of Nb-rich amorphous phase (appear dark). *Insets* show the electron diffraction pattern and the radial distribution of scattered electrons

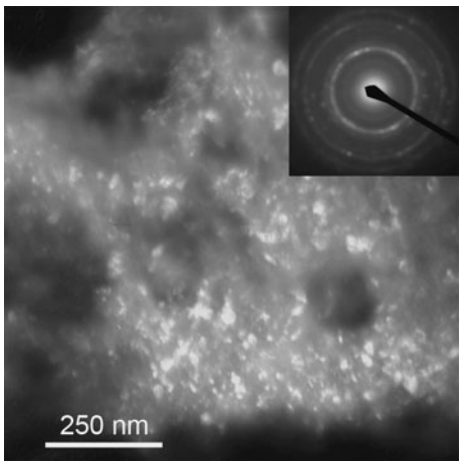

Fig. 5 Dark-field TEM micrograph of the $Ni_{50}Nb_{20}Y_{30}$ alloy after HPT taken from a predominantly crystalline area. *Inset* shows the electron diffraction pattern. The dark-field micrograph was taken using one of the reflections of a NiY crystalline phase

where the radial distribution of scattered electrons is shown). The peak positions ($q_{1e} = 25.7\ nm^{-1}$ and $q_{2e} = 29.5\ nm^{-1}$) correspond to those in the XRD spectrum ($q_{1x} = 25.1\ nm^{-1}$ and $q_{2x} = 28.8\ nm^{-1}$). Though two halos were observed in the XRD spectrum, they were not resolved in the SAED pattern due to the lower angular resolution of this method. Nevertheless, the contrast between the two different amorphous phases is visible. Figure 5 shows a dark-field image of a crystalline part of the sample. The corresponding SAED pattern is shown in the inset. The diffraction rings in this pattern are from the

NiY phase. The size of the NiY grains is about 20 nm, which is consistent with the XRD data.

Figure 4 shows that the amorphous region contains two different amorphous phases, seen as dark and bright. This contrast appears to arise from the different densities of the two amorphous phases. Similar to previous work [49–51], the dark regions are Nb rich whereas the bright regions are Y rich, since the atomic weight of niobium is higher than that of yttrium, similar to the contrast observed previously [48–52]; such an interpretation of the TEM pattern contrast is supported by the XRD analysis. Alternatively, this bright–dark contrast of the amorphous materials may appear due to lower density in slip bands after deformation [70]. However, in this case, the morphology of the dark and bright zones and the microstructure differs a lot from that shown in Fig. 4.

We now discuss and describe the morphology, spatial distribution, and topology of the mixture of two amorphous phases. In the case of conventional GB wetting, the liquid phase can completely separate solid grains from each other, forming a continuous intergranular layer (so-called complete wetting with zero contact angle at the GB). Otherwise, a liquid phase forms an array of liquid inclusions or droplets between grains (incomplete wetting with nonzero contact angle). In the case of incomplete wetting, neighboring grains partially contact each other. Indeed, finely mixed layers and grains of two different amorphous phases are visible in thin areas of the sample (Fig. 4). Fine, 5–10 nm, round bubbles of bright amorphous phase are embedded in the darker "grains" (they are really bubbles, since only sphere-shaped rather than rod-shaped "particles" are visible in Fig. 4). Such small bubbles of Y-rich amorphous phase are indicated in the left part of Fig. 4 by two white arrows.

The bright "bubbles" are seen more clearly in thinner portions of the TEM sample. In thicker portions of the sample, multiple, 5–10 nm "bubbles" superimpose and become less visible. The dark Nb-rich amorphous phase (indicated by the X in Fig. 4) separates all spherical areas of the bright phase from each other. Bubbles of the bright phase do not form contacts with neighboring bright grains, even when the distance between them is very small. This means that the dark amorphous phase prevents the bright phase from forming contacts, as it would do if it completely wetted the possible "GBs" between the bright grains. Such GBs would form if the bubbles of the bright phase grew together, as for amorphous particles formed individually from the gas phase [9, 10].

The dark "matrix" grains are slightly elongated with size of 20–200 nm. The dark grains of Nb-rich amorphous phase (marked by the X) are in turn separated by thin layers of the bright amorphous phase. Two such layers of Y-rich phase (a few nanometers thick) between the large grains of Nb-rich phase are shown by white arrows in the bottom part of Fig. 4. This can be interpreted as indicating that the bright phase also completely wets the GBs between dark areas. This situation is similar to the wetting of conventional GBs by a second solid phase [20–23]. This second solid phase can also contain GBs, which can, in turn, be completely wetted by the first phase. In such a case, the microstructure would contain only interphase boundaries but no GBs.

This microstructure radically differs from that obtained by melt-spinning [49–51]. The heterogeneities in phase-separated amorphous metallic alloys obtained by quenching from the melt range in size from nanometers to micrometers, exhibiting features of self-similarity [48–52]. In other words, the bright phase contains spherical dark regions, which in turn contain smaller bright spheres, and so on. Such Russian *matreshka*-doll-like structure forms as a result of sequential formation of Nb- and Y-rich phases during cooling of the melt in the dome-like immiscibility area, which broadens with decreasing temperature [49].

Among the three elements in the investigated ternary Ni–Nb–Y alloy, the Ni–Nb and Ni–Y couples have considerable negative mixing enthalpy (about −40 kJ/mol for $Ni_{50}Nb_{50}$ [71] and −28 kJ/mol for $Ni_{80}Y_{20}$ [72]). This negative mixing enthalpy indicates the presence of intermetallic bonds between atoms in the mixture. On the other hand, the mixing enthalpy for the Nb–Y couple is positive (about +35 kJ/mol [73]), which is the reason for the separation of the Ni–Nb–Y alloys into Nb- and Y-rich phases. As a result, during solidification, a polycrystalline alloy forms, predominantly consisting of two phases, namely NiY and Ni_3Nb. The binary Ni–Nb and Ni–Y phase diagrams contain also other intermetallic phases.

In the ideal NiY phase, each Ni and/or Y atom is surrounded by eight atoms. The first coordination sphere consists of atoms of the other element. In the Ni_3Nb compound, each Nb atom is surrounded by 12 Ni atoms. It is reasonable to suppose that compositional fluctuations take place in Nb-doped NiY. In such a lattice, some Y atoms are substituted by Nb, enabling formation of Ni–Nb clusters. At the same time, the Y and Nb atoms have the tendency to repel each other. In the liquid state, clusters exist where Y and/or Nb atoms are surrounded predominantly by Ni atoms. Such clusters can have different configurations and coordination numbers. During rapid crystallization, Ni–Nb and Ni–Y clusters in the NiY lattice acquire configuration consistent with its translational invariance, but the compositional order of the lattice is disturbed. Such compositional fluctuations are generated also by inclusion of Ni–Y clusters in the Ni_3Nb lattice. The magnitude of such compositional fluctuation is determined by the crystallization rate. Recovery of such compositional short-range order is hindered by the large size of the Y ions.

It is known that SPD leads to formation of nanocrystalline structures in various materials [74, 75]. The grain refinement behavior is controlled by the processes of dislocation glide and disclination rotation. This results in self-similarity with increasing deformation, and the mean grain size attains a certain value of about 0.1 μm. At this deformation stage, a dynamic equilibrium appears, and the average density of the extended structural defects (dislocations, disclinations, and GBs) reaches a steady-state value.

The Ni–Nb–Y alloy is a multiphase polycrystalline material after solidification from the liquid state. Its crystallites (grains) exhibit large compositional fluctuations determined by the short-range compositional ordering. Retention of different types of short-range compositional order turns out to be energetically favorable during melt crystallization. Such retention takes place during local deformation, restoring translational invariance but not the compositional order.

Formation of trans-crystallite shear bands begins during the deformation. Along with formation of extended structural defects, this leads to destruction of the short-range compositional order in these bands. Since the topological order is also destroyed in these shear bands, this makes recovery of the short-range compositional order through migration of small atoms (Ni atoms in our case) both possible and energetically favorable. Rearrangements taking place in the material are accumulated during this recovery. These rearrangements can possess different topological order, including also clusters with noncrystalline atomic arrangement, resulting in amorphization of crystallites adjacent to the shear band. The energy of plastic deformation serves as a driving force for this amorphization process, therefore amorphization can advance into the crystallites during successive deformation cycles. Amorphization initiation induced by compositional disorder has been observed in computational experiments [76–80].

The existence of amorphous alloy with a stable, self-similar heterophase structure is of particular interest. To clarify this issue, note that a mixed diffusive–viscous flow can arise in multicluster bulk metallic glasses due to the effect of external stresses. Together with diffusive transfer along intercluster interfaces, this flow can give rise to cluster refinement due to trans-cluster shear [78]. Results of experimental investigation and description of this deformation mode can be found elsewhere [78]. It is important to note that the viscosity of the amorphous phase decreases significantly during mixed diffusive–viscous flow due to the acceleration of structural relaxation under the external stress. The mean cluster size in the investigated initial glass was about 10 nm [78]. This assessment gives an impression of a typical limiting scale of amorphous structure refinement.

In the amorphous alloy with separated amorphous phases, two processes take place during deformation, i.e., cluster refinement and mixing of clusters with different composition. Qualitatively, it is clear that more rigid clusters (in our case Ni–Nb) have to be divided by a more pliable phase with lower viscosity (i.e., Ni–Y). In so doing, the complete wetting condition should be fulfilled. So, the more pliable and less viscous phase plays the role of a wetting GB phase, as found earlier in polycrystalline alloys [16–19].

Conclusions

SPD of $Ni_{50}Nb_{20}Y_{30}$ alloy by high-pressure torsion enables the production of alloys containing two different coexisting amorphous phases (as well as crystalline phases). The topology of the spatial distribution of the two amorphous phases permits one to speak about mutual wetting of "GBs" in one amorphous phase by the layers of another amorphous phase.

Acknowledgements The authors thank the Russian Foundation for Basic Research (contracts 09-08-90469, 11-02-90429) and Ukrainian Fundamental Research State Fund (contract Ф28.2107) for financial support of investigations and exchange travel.

References

1. Gottstein G, Shvindlerman LS (2009) Grain boundary migration in metals, thermodynamics, kinetics, applications, 2nd edn. CRC Press, Boca Raton
2. Bakai AS (1987) Polycluster amorphous solids. Energoatomizdat, Moscow (In Russian)
3. Bakai AS (1994) In: Beck H, Guntherodt H-J (eds) Glassy Metals III. Springer, Heidelberg, p 209
4. Bakai AS, Bakai SA, Eckert J et al (2007) J Non-Cryst Solids 32(40):3754
5. Pozdnyakov VA, Glezer AM (2002) Phys Solid State 44(4):732
6. Pozdnyakov VA, Glezer AM (2002) Dokl Phys 47:852
7. Pozdnyakov VA, Glezer AM (2005) Phys Solid State 47:817
8. Kolesnikova AL, Ovid'ko IA, Romanov AE (1999) Phys Solid State 41:1491
9. Averback RS, Hahn H, Höfler HJ et al (1990) Appl Phys Lett 57:1745
10. Würschum R, Rollinger M, Kisker H et al (1995) Nanostruc Mater 6:377
11. Cahn JW (1977) J Chem Phys 66:3667
12. Ebner C, Saam WF (1977) Phys Rev Lett 38:1486
13. Passerone A, Eustathopoulos N, Desré P (1977) J Less-Common Met 52:37
14. Passerone A, Sangiorgi R, Eustathopoulos N (1982) Scr Metall 16:547
15. Eustathopoulos N (1983) Int Met Rev 28:189
16. Straumal BB (2003) Grain boundary phase transitions. Nauka, Moscow (In Russian)
17. Straumal B, Muschik T, Gust W et al (1992) Acta Metall Mater 40:939
18. Straumal B, Molodov D, Gust W (1995) Interface Sci 3:127

19. Straumal B, Gust W, Watanabe T (1999) Mater Sci Forum 294(296):411
20. López GA, Mittemeijer EJ, Straumal BB (2004) Acta Mater 52:4537
21. Straumal BB, Gornakova AS, Kogtenkova OA et al (2008) Phys Rev B 78:054202
22. Straumal BB, Baretzky B, Kogtenkova OA et al (2010) J Mater Sci 45:2057. doi:10.1007/s10853-009-4014-6
23. Straumal BB, Kogtenkova OA, Straumal AB et al (2010) J Mater Sci 45:4271. doi:10.1007/s10853-010-4377-8
24. Avishai A, Scheu C, Kaplan WD (2003) Z Metallkd 94:272
25. Avishai A, Kaplan WD (2004) Z Metallkd 95:266
26. Nosova GI, Shalimova AV, Sundeev RV et al (2009) Cryst Rep 54:1058
27. Xie GQ, Ohashi O, Yamaguchi N et al (2002) Mater Trans 43:2177
28. Straumal BB, Mazilkin AA, Protasova SG et al (2009) Phys Rev B 79:205206
29. Chou C-P, Turnbull DJ (1975) Non-Cryst Solids 17:169
30. Chen HS (1976) Mater Sci Eng 23:151
31. Marcus M (1979) J Non-Cryst Solids 30:317
32. Doi K, Kayano H, Masumoto T (1978) J Appl Cryst 11:605
33. Tanner L, Ray R (1980) Scr Metall 14:657
34. Yavari AR (1986) Int J Rapid Solidif 2:47
35. Inoue A, Yamamoto M, Kimura HM et al (1987) J Mater Sci 6:194. doi:10.1007/BF01728983
36. Abrosimova GE, Aronin AS, Voropaeva LV (1989) Metallofizika 11(3):102 (in Russian)
37. Yavari AR (1988) Acta Metall 36:1863
38. Inoue A, Chen S, Masumoto T (1994) Mater Sci Eng A 179(180):346
39. Walter J (1977) Mater Sci Eng 29:161
40. Abrosimova GE, Aronin AS (1998) Phys Sol State 40:1603
41. Abrosimova GE, Aronin AS, Ignat'eva EY et al (1999) JMMM 203:169
42. Abrosimova G, Aronin A, Ignatieva E (2007) Mater Sci Eng A 449–451:485
43. Wang XD, Bednarcik J, Saksi K et al (2007) Appl Phys Lett 91:081913
44. Stoica M, Das J, Bednarcik J et al (2008) J Appl Phys 104:013522
45. Abrosimova GE, Aronin AS, Afonikova NS et al (2010) Phys Sol State 52:1892
46. Abrosimova G, Aronin A, Barkalov OO et al. (2011) Phys Sol State 53:229
47. Kündig AA, Ohnuma M, Ping DH et al (2004) Acta Mater 52:2441
48. Mattern N, Kühn U, Gebert A et al (2005) Scr Mater 53:271
49. Mattern N, Kühn U, Gebert A et al (2007) Mater Sci Eng A 449(451):207
50. Mattern N (2007) J Non-Cryst Solids 353:1723
51. Mattern N, Gemming T, Goerigk G et al (2007) Scr Mater 57:29
52. Concustell A, Mattern N, Wendrock H et al (2007) Scr Mater 56:85
53. Mattern N, Zinkevich M, Loser W et al (2008) J Phase Equilib Diffus 29:141
54. Mattern N, Goerigk G, Vainio U et al (2009) Acta Mater 57:903
55. Mattern N, Gemming T, Thomas J et al (2010) J Alloys Comp 495:299
56. Park BJ, Chang HJ, Kim DH et al (2004) Appl Phys Lett 85:6353
57. Jayaraj J, Park JM, Gostin PF et al (2009) Intermetal 17:1120
58. Park BJ, Sohn SW, Kim WT et al (2009) J Alloys Comp 483:260
59. Park ES, Kyeong JS, Kim DH (2007) Scr Mater 57:49
60. Park ES, Jeong EY, Lee J-K et al (2007) Scr Mater 56:197
61. Louzguine-Luzgin DV, Seki I, Yamamoto T et al (2010) Phys Rev B 81:144202
62. Louzguine-Luzgin DV, Wada T, Kato H et al (2010) Intermetall 18:1235
63. Wada T, Louzguine-Luzgin DV, Inoue A (2007) Scr Mater 57:901
64. Straumal BB, Mazilkin AA, Protasova SG et al (2011) Kovove Mater—Metal Mater 49:17
65. Dinnebier RE (ed) (2008) Powder diffraction. RSC, Cambridge
66. Kattner UR (1997) JOM 49:14
67. Villars PC, Lauriston D, Pearson WB (1996) Handbook of lattice spacings and structures of metals and alloys. American Soc Metals, Materials Park, OH
68. JSPDS Database (2001) International Centre for Diffraction Data, Newtown Square, PA
69. Mazilkin AA, Straumal BB, Rabkin E et al (2006) Acta Mater 54:3933
70. Abrosimova GE, Aronin AS, Dobatkin SV et al (2008) Phys Met Metallogr 106:597
71. Xia L, Li WH, Fang SS et al (2006) J Appl Phys 99:026103
72. Batalin GI, Stukalo VA, Neshchimenko N et al (1977) Izv Akad Nauk SSSR Metal 6:44
73. Park ES, Chang HJ, Kyeong JS et al (2008) JMR 23:1995
74. Valiev RZ, Islamgaliev RK, Alexandrov IV (2000) Progr Mater Sci 45:103
75. Valiev RZ, Estrin Y, Horita Z et al (2006) JOM 58:33
76. Massobrio C, Pontikis V, Martin G (1989) Phys Rev Lett 62:1142
77. Massobrio C, Pontikis V, Martin G (1990) Phys Rev B 41:10486
78. Massobrio C, Pontikis V (1992) Phys Rev B 45:2484
79. Evangelakis GA, Pontikis V (2009) J Alloys Comp 483:662
80. Abrosimova GE, Aronin AS (2009) Phys Sol State 51:1765